Supplemental Material for "NV-Diamond Magnetic Microscopy using a Double Quantum 4-Ramsey Protocol"

Connor A. Hart,[1,2,3,4] Jennifer M. Schloss,[5,6,7] Matthew J. Turner,[1,2,3,4,7]
Patrick J. Scheidegger,[8] Erik Bauch,[9] and Ronald L. Walsworth[1,2,3,4,7,9]

[1] *Department of Physics, Harvard University, Cambridge, Massachusetts 02138, USA*
[2] *Department of Computer and Electrical Engineering, University of Maryland, College Park, MD 20740, USA*
[3] *Department of Physics, University of Maryland, College Park, MD 20740, USA*
[4] *Quantum Technology Center, University of Maryland, College Park, MD 20740, USA*
[5] *Lincoln Laboratory, Massachusetts Institute of Technology, Lexington, Massachusetts 02420, USA*
[6] *Department of Physics, Massachusetts Institute of Technology, Cambridge, Massachusetts 02138, USA*
[7] *Center for Brain Science, Harvard University, Cambridge, Massachusetts 02138, USA*
[8] *Department of Physics, ETH Zurich, 8093 Zurich, Switzerland*
[9] *Harvard-Smithsonian Center for Astrophysics, Cambridge, Massachusetts 02138, USA*

(Dated: April 5, 2021)

CONTENTS

S1. Crystal Stress Terms in the Ground State NV$^-$ Hamiltonian 1

S2. Sources of Microwave Pulse Errors 3

S3. Generalized 4-Ramsey Phase Requirements 3

S4. SQ and DQ 2-Ramsey Protocols 3

S5. Ramsey Imaging Using the heliCam C3 Lock-in Camera 4

S6. Ramsey Fringe Imaging 6

S7. Per-Pixel Allan Deviation 6

S8. Averaged Magnetic Images 7

References 10

S1. CRYSTAL STRESS TERMS IN THE GROUND STATE NV$^-$ HAMILTONIAN

In this section, we describe the effect of crystal stress on the NV$^-$ ground state spin resonances. The ground state spin Hamiltonian for a chosen NV$^-$ orientation in the presence of crystal stress and a static (bias) magnetic

field is given by [S1–S3]:

$$\begin{aligned} H/h \approx & \left(D + M_z\right) S_z^2 + \frac{\gamma}{2\pi} \vec{B} \cdot \vec{S} \\ & + M_x \left(S_y^2 - S_x^2\right) \\ & + M_y \left(S_x S_y + S_y S_x\right) \\ & + N_x \left(S_x S_z + S_z S_x\right) \\ & + N_y \left(S_y S_z + S_z S_y\right). \end{aligned} \tag{S1}$$

Here the z axis is defined along the NV$^-$ symmetry axis, $D \approx 2870$ MHz is the zero-field splitting, S_i are the dimensionless spin-1 projection operators, $\gamma/2\pi = g_{NV}\mu_B/h \approx 28.03\,\mathrm{GHz/T}$ is the NV$^-$ gyromagnetic ratio, $\vec{B}$ is the magnetic field, and M_i and N_i are terms related to crystal stress. In the following analysis, we do not include the N_i terms or contributions due to transverse magnetic fields, which are suppressed by the zero-field splitting [S1–S5].

The projection of the magnetic field along the NV$^-$ symmetry axis is indicated by B_z. We refer to M_z as the axial crystal stress and define the transverse crystal stress, $M_\perp$, as $-(M_x + iM_y)$. Using these definitions, Eq. S1 can be rewritten, in matrix form, as:

$$H/h = \begin{pmatrix} D + M_z + \frac{\gamma}{2\pi} B_z & 0 & M_\perp \\ 0 & 0 & 0 \\ M_\perp^* & 0 & D + M_z - \frac{\gamma}{2\pi} B_z \end{pmatrix}. \tag{S2}$$

For non-zero M_z and $M_\perp$, the energy eigenvalues of the NV$^-$ Hamiltonian (Eq. S2) for the $|\pm 1\rangle$ states become

$$E_{|\pm 1\rangle}/h = D + M_z \pm \sqrt{\left(\frac{\gamma}{2\pi} B_z\right)^2 + ||M_\perp||^2} \tag{S3}$$

$$\approx D + M_z \pm \left[\frac{\gamma}{2\pi} B_z + \frac{||M_\perp||^2}{2\frac{\gamma}{2\pi} B_z} + \mathcal{O}\left(\frac{||M_\perp||^4}{B_z^2}\right)\right]. \tag{S4}$$

To first order, crystal stress shifts the energies of the $|\pm 1\rangle$ states in common mode via the axial-stress term M_z. Single quantum (SQ) measurements, which probe the difference between $E_{|0\rangle}$ and either $E_{|\pm 1\rangle}$, are vulnerable to these axial-stress-induced shifts. Conversely, double quantum (DQ) measurements, which probe the difference between $E_{|+1\rangle}$ and $E_{|-1\rangle}$, are insensitive to axial stress.

At second order, the transverse crystal stress term $M_\perp$ induces magnetic-like, differential shifts in the energy eigenvalues $E_{|\pm 1\rangle}$, which are not mitigated in either the SQ or DQ sensing bases. However, these transverse-stress-induced shifts are suppressed by a factor $||M_\perp||/(\gamma B_z/\pi)$ where, as noted earlier, B_z is the projection of $\vec{B}$ along a particular NV$^-$ orientation. In the present work, if we assume variations in $M_z \approx M_\perp \approx 100\,\mathrm{kHz}$, then the aligned bias magnetic field of 5 mT in the present experiment provides a suppression of ≈ 450. The resultant shift of 0.2 kHz (for $M_\perp = 100\,\mathrm{kHz}$) is approximately equivalent to a magnetic field of 8 nT – sufficiently small to be negligible compared to the axial-stress-induced shifts that dominate the SQ measurements presented in the main text. As apparent from the above analysis, the effects of transverse stress inhomogeneity can be further suppressed by increasing B_z.

S2. SOURCES OF MICROWAVE PULSE ERRORS

Spatial Rabi Gradients – Figure 1(c) in the main text depicts the Rabi gradient for a mm-scale shorted coaxial loop. Although the spatial properties of the applied MW field depend upon setup-specific synthesis and delivery approaches, the ±4% (±200 kHz) gradient on top of an average Rabi frequency $\Omega_{\text{avg}} = 5$ MHz shown in the main text is typical.

Hyperfine Splitting-Induced Detunings – The NV$^-$ hyperfine splitting can also introduce MW pulse errors as a result of the detuning-dependent effective Rabi frequency Ω_{eff}. Samples grown with the naturally abundant, ^{14}N nitrogen isotope ($I = 1$) are particularly vulnerable because any single-tone MW field is detuned from at least two of the three hyperfine-split resonances. The effective Rabi frequency is given by $\Omega_{\text{eff}} = \sqrt{\Omega^2 + \Delta^2}$, where Ω is the on-resonance Rabi frequency and Δ is the detuning from a particular hyperfine resonance. In this work, the MW pulse errors induced by the hyperfine splitting ($\Omega_{\text{avg}} = 5$ MHz, $\Delta \approx 2.2$ MHz) result in effective Rabi frequencies of $\Omega_{\text{eff}} = 5 \pm 0.46$ MHz for the two detuned hyperfine resonances ($m_I = \pm 1$), approximately double the Rabi gradient of ±200 kHz. Potential approaches to mitigate hyperfine-induced pulse errors include increasing the MW Rabi frequency, implementing pulse envelope shaping, or operating equally detuned from the two hyperfine split resonances of isotopically-purified ^{15}N ($I = 1/2$). All three of these directions present challenges, adding experimental complexity or requiring changes to the CVD synthesis process.

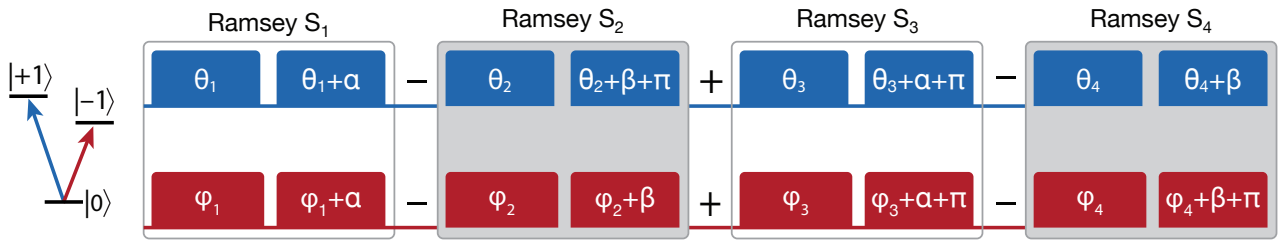
Stress-Induced Detunings – Finally, axial-stress-induced shifts in the NV$^-$ resonance frequencies can also result in effective Rabi frequency variations. Using the values reported in Sec. IV as an estimate ($|D_{90} - D_{10}| = 280\,(14)$ kHz), the effective Rabi frequency deviates from $\Omega_{\text{avg}} = 5$ MHz by only about 10 kHz. However, in pixels with larger stress-induced shifts, the effect would become comparable to the two other sources described above.

S3. GENERALIZED 4-RAMSEY PHASE REQUIREMENTS

We describe here the generalized phase requirements for the DQ 4-Ramsey protocol (refer to Fig. S1). First, only the relative phase shifts between the two MW tones addressing the $|0\rangle \rightarrow |-1\rangle$ and $|0\rangle \rightarrow |+1\rangle$ transitions are critical to the DQ 4-Ramsey protocol. As a consequence, the phases θ_i and ϕ_i in Fig. S1 can be selected arbitrarily for the initial two-tone MW pulse in the each sequence S_i. The choices of α and β for the final MW pulses in each sequence can also be chosen without restriction (in the main text: $\alpha = \beta = 0$). However, subsequent MW pulses must have a specific phase relationship across S_{1-4} as depicted in Fig S1 by the π phase shifts for select pulses. Second, the order of S_{1-4} can be permuted. For example, S_1 and S_3 may be swapped without altering $S_{4R} = S_1 - S_2 + S_3 - S_4$. In this work, the form of S_{4R} was chosen to be compatible with the pixel-by-pixel, lock-in detection scheme of the heliCam C3 camera (see Supplemental Sec. S5).

S4. SQ AND DQ 2-RAMSEY PROTOCOLS

This section provides additional details on the conventional SQ and DQ 2-Ramsey phase alternation protocols. The SQ 2-Ramsey single-channel (photodiode) data presented in Fig. 3(b) and 3(d) in the main text is calculated



Supplemental Figure S1. Generalized phase requirements for the DQ 4-Ramsey protocol. The phases for α, β, θ_i, and ϕ_i for $i = 1 - 4$ may be chosen arbitrarily. S_1 and S_3 yield DQ signals which differ in sign from S_2 and S_4 when sensing the same magnetic field.

using the visibility $S_{2R} = (S_1 - S_2)/(S_1 + S_2)$ where S_i indicates the signal produced by measurement $i = 1, 2$. As defined above, S_{2R} suppresses noise sources that vary slowly compared to the time over which S_1 and S_2 are acquired [S6]. In contrast, when the SQ 2-Ramsey protocol is implemented using the heliCam C3 camera, only the numerator of S_{2R} is accessible (see further discussion in Supplemental Sec. S5).

As with the SQ results, the single-channel (photodiode) DQ 2-Ramsey data presented in Fig. 3(b) and 3(d) in the main text is also calculated according to the visibility $S_{2R} = (S_1 - S_2)/(S_1 + S_2)$. The MW pulse phases chosen for the DQ 2-Ramsey measurements are identical to those of the first two Ramsey signals (S_1 and S_2) in the 4-Ramsey protocol.

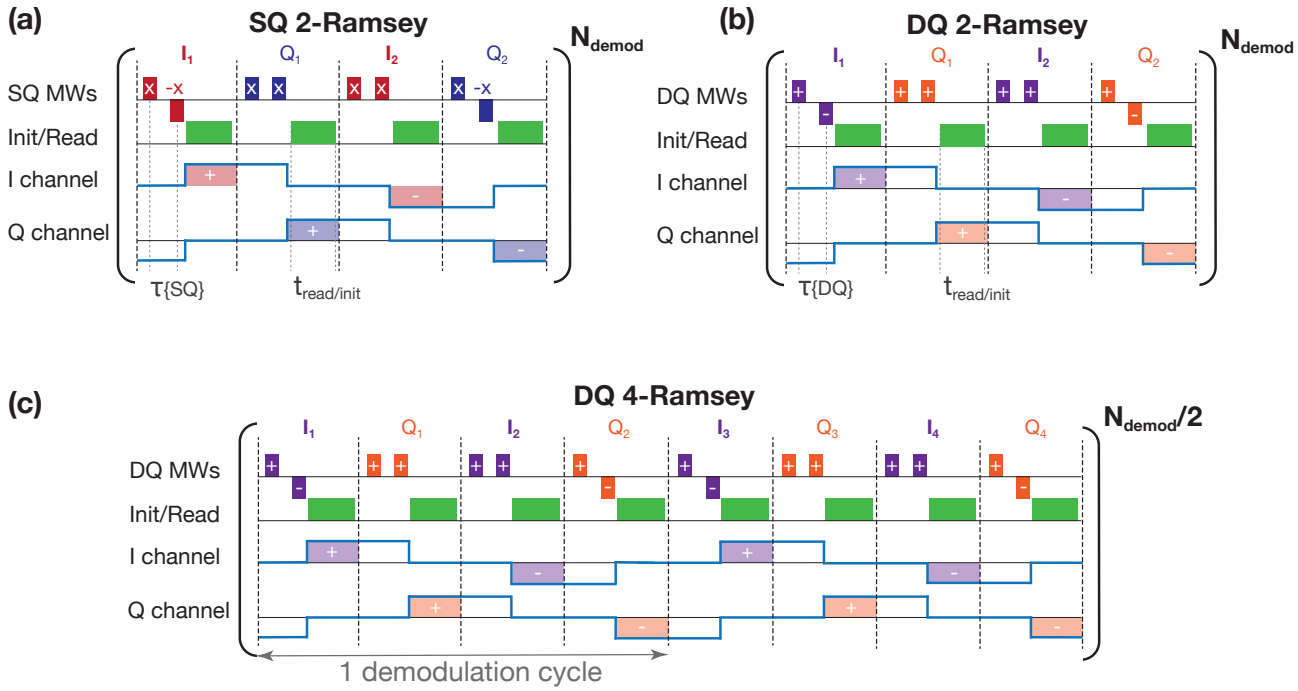
Comparing the DQ 2-Ramsey and 4-Ramsey representations in Fig. 2(b,c) of the main text, it is apparent that calculating S_{2R} requires half the number of Ramsey signals as S_{4R}. For implementations where each Ramsey measurement is accessible, the bandwidth of the 2-Ramsey protocols is thus a factor of two greater than that of the 4-Ramsey protocol. However, because the DQ 4-Ramsey protocol acquires Ramsey signals at the same rate as the DQ 2-Ramsey protocol (which all add constructively), there is no corresponding impact on the magnetic sensitivity. Additionally, if desired, the 4-Ramsey data could be post-processed as 2-Ramsey data using S_{2R} to recover the sacrificed bandwidth.

S5. RAMSEY IMAGING USING THE HELICAM C3 LOCK-IN CAMERA

The heliCam C3 operates by subtracting alternating exposures in analog detection; and then digitizing the background-subtracted signal, enabling the detected magnetic field information to fill each pixel's 10-bit dynamic range. Each frame from the camera contains the accumulated difference signal for multiple exposure pairs. The device is capable of operating at internal demodulation frequencies of up to 250 kHz (exposure rates of up to 1 MHz).

The demodulation frequency can be defined by a user-input demodulation signal (square wave) with each demodulation cycle broken into four quarters. The exposures from the first and third quarters subtract to produce an in-phase image on the camera's I channel. Similarly, the exposures from the second and fourth quarters subtract to produce a quadrature image on the camera's Q channel. The output from the camera

consists of these two images per frame. Since each demodulation cycle includes four exposures, the internal exposure rate is $4 \times F_{\mathrm{demod}}$ where F_{demod} indicates the inverse of one demodulation cycle period.



Supplemental Figure S2. **Schematics of measurement protocols used for magnetic imaging.** **(a)** A single quantum (SQ) 2-Ramsey protocol is shown synchronized with detection by the heliCam C3 lock-in camera. The single demodulation cycle depicted is repeated $\mathrm{N_{demod}}$ times within each frame. Two SQ 2-Ramsey (red and blue pulses) protocols are interwoven to generate images on the I and Q channels. The camera exposures (shaded regions on the I and Q channels) are chosen to collect the fluorescence from the optical readout/initialization pulses (green pulses). The optical pulses are contained within the exposure duration. For optimal magnetic sensitivity, the Ramsey sensing duration, $\tau\{\mathrm{SQ}\} = 910\,\mathrm{ns}$, is approximately the median $T_2^*\{\mathrm{SQ}\}$ across the field of view. The duration of the combined readout and initialization optical pulses ($t_{\mathrm{init/read}} = 4\,\mu\mathrm{s}$) is experimentally determined to yield the optimal magnetic sensitivity. **(b)** Schematic of a DQ 2-Ramsey protocol. The optimal sensing duration is approximately given by the median $T_2^*\{\mathrm{DQ}\}$ ($\tau\{\mathrm{DQ}\} = 662\,\mathrm{ns}$). **(c)** Schematic of a double quantum (DQ) 4-Ramsey protocol implemented on the helicam. The two DQ 4-Ramsey protocols (orange and purple pulses), which are interwoven to generate images on the I and Q channels, span two demodulation cycles. However, the total number of demodulation cycles per frame remains constant compared to the 2-Ramsey protocols.

The I and Q images produced during each frame contain the accumulated difference signal from N_{demod} repetitions of the demodulation cycle described above. In the present work, the typical number of demodulation cycles ($N_{\mathrm{demod}} = 24$) and demodulation rates ($F_{\mathrm{demod}} \approx 35\,\mathrm{kHz}$) result in external frame rates (F_{S}) of approximately 1.5 kHz. The maximum external frame rate of the camera is 3.8 kHz. Note that in the main text, the exposure rate of ($4 \times F_{\mathrm{demod}} \approx 140\,\mathrm{kHz}$) is referenced instead of F_{demod}.

For the magnetic sensitivity discussion in Sec. V, the SQ and DQ external frame rates differ slightly ($F_S\{\mathrm{SQ}\} = 1.45\,\mathrm{kHz}$ versus $F_S\{\mathrm{DQ}\} = 1.5\,\mathrm{kHz}$) because the optimal sensing duration is approximately given by the median T_2^* and therefore depends upon the sensing basis ($\tau\{\mathrm{SQ}\} = 910\,\mathrm{ns}$ and $\tau\{\mathrm{DQ}\} = 662\,\mathrm{ns}$). Additionally, accounting for the four optical pulses ($t_{\mathrm{init/read}} = 4\,\mu\mathrm{s}$ each), four pairs of microwave pulses ($< 1\,\mu\mathrm{s}$ per cycle), and delays between control pulses ($8\,\mu\mathrm{s}$ per cycle), the duration of each demodulation cycle, t_{demod}, is $28.7\,\mu\mathrm{s}$ ($27.8\,\mu\mathrm{s}$) for the SQ (DQ) measurements.

Figure S2 depicts the implementation of pulsed NV^- readout using the heliCam in further detail. The MW and optical control pulses are synchronized with the camera's I and Q exposures. Two protocols are interleaved such that both the I and Q channels produce images with the proper phase alternation (e.g. SQ 2-Ramsey, DQ 2-Ramsey, DQ 4-Ramsey). Additionally, the MW pulse phases for the Q channel are chosen such that the Q channel contains the negative magnetic signal compared to the I channel image. S_I is then subtracted from S_Q to yield a single image per frame.

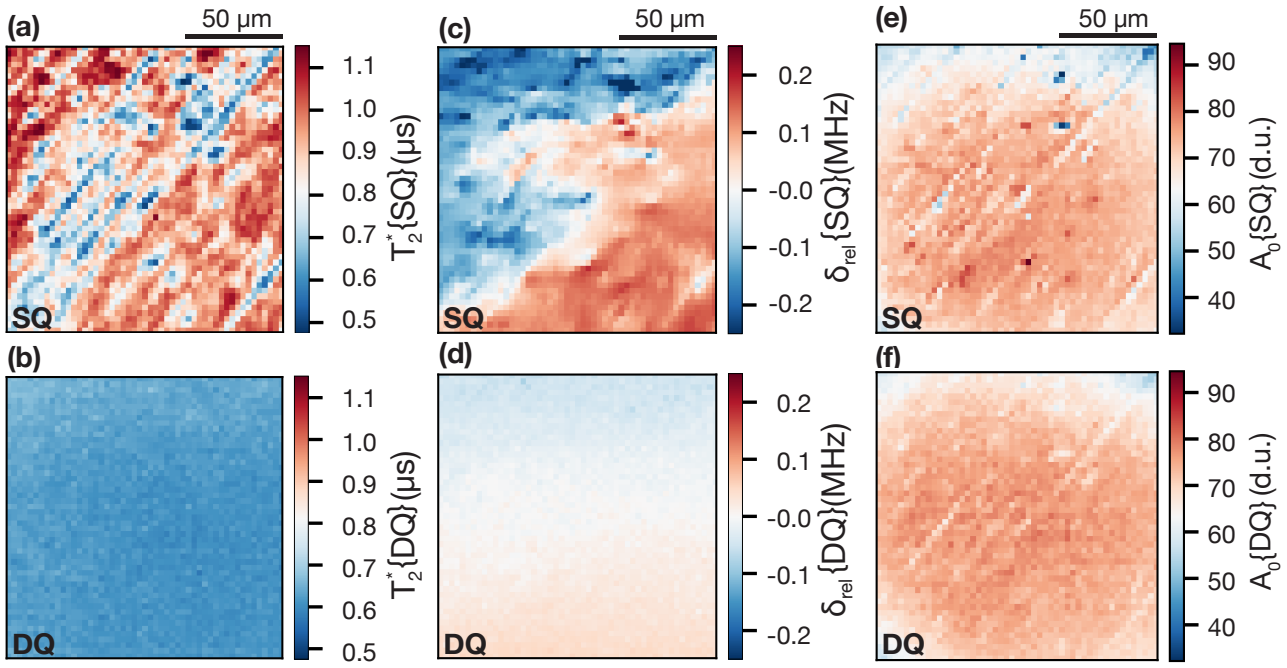
While a full 2-Ramsey protocol requires only one demodulation cycle, compared to two cycles for the 4-Ramsey protocol, the total number of demodulation cycles per frame is fixed to $N_{\mathrm{demod}} = 24$ for both the 2-Ramsey and 4-Ramsey protocols. As a consequence, the SQ and DQ frame rates are the same (neglecting the few percent change due to the basis-dependent sensing interval). Additionally, the difference signals between exposure pairs add constructively for the duration of the frame. Thus, the choice of protocol does not impact bandwidth or sensitivity when using the heliCam C3.

S6. RAMSEY FRINGE IMAGING

In Figs. S3(a)-S3(d), the SQ and DQ dephasing times T_2^* and relative resonance shifts δ_{rel} are reproduced from Fig. 3 in the main text. In addition, the extracted A_0 fringe amplitudes for the SQ and DQ sensing bases are shown in Figs. S3(e) and S3(f). As noted in the main text, the extracted amplitudes A_i (indexed by $m_I = -1, 0, 1$) for the measured Ramsey fringes are proportional to the measurement contrast and reported in digital units (D.U.). The comparable median amplitudes of $A_0\{\mathrm{SQ}\}$ and $A_0\{\mathrm{DQ}\}$ (72.1 and 73.5 in digital units as reported by the camera) and relative inter-decile ranges (21 % and 14 %) are largely due to the Gaussian intensity profile of the excitation beam and fixed exposure duration. Shorter length-scale spatial variations ($< 50\,\mu\mathrm{m}$) in the extracted SQ amplitude exhibit a strong correlation with images of the $T_2^*\{\mathrm{SQ}\}$ and relative resonance shifts $\delta_{\mathrm{rel}}\{\mathrm{SQ}\}$ due to stress gradients decreasing the ODMR contrast and inducing variations in the effective Rabi frequency.

S7. PER-PIXEL ALLAN DEVIATION

For the magnetic sensitivities reported in the main text and depicted in Fig. 4, SQ 2-Ramsey and DQ 4-Ramsey data was collected, each for 1 second of measurement time and neglecting the overhead time required to transfer data from the camera to the computer. Allan deviations calculated using similar SQ 2-Ramsey and DQ 4-Ramsey measurements (with greater than 1 s of data) are shown in Fig. S4 for 50 randomly selected pixels across the same field of view presented in the main text. For both measurement protocols, the Allan deviation exhibits a



Supplemental Figure S3. **Imaging NV⁻ Ensemble Spin Properties.** **(a)** Image of the single quantum (SQ) T_2^* extracted by fitting the Ramsey free induction decay to Eq. 4 in the main text. The field of view is 125 μm by 125 μm. Spatial variations in $T_2^*\{\mathrm{SQ}\}$ are attributed to stress-induced broadening of the NV⁻ resonances within the 3-dimensional volume imaged onto a pixel. **(b)** Image of the double quantum $T_2^*\{\mathrm{DQ}\}$ measured using the 4-Ramsey protocol across the same field of view as shown in (a). In pixels, with minimal stress gradients, the $T_2^*\{\mathrm{DQ}\}$ is half the $T_2^*\{\mathrm{SQ}\}$, as expected, due to the effectively doubled dipolar coupling to the surrounding paramagnetic spin bath [S7], which dominates NV⁻ dephasing. **(c)** Image of the relative SQ resonance shifts $\delta_{\mathrm{rel}}\{\mathrm{SQ}\}$ away from the median SQ Ramsey fringe frequency f_{SQ}. Variations in $\delta_{\mathrm{rel}}\{\mathrm{SQ}\}$ are attributed to axial-stress-induced shifts of the NV⁻ resonance frequencies between pixels. **(d)** Image of the relative DQ detuning $\delta_{\mathrm{rel}}\{\mathrm{DQ}\}$. The axial-strain-induced shifts apparent in (c) are mitigated. Inhomogeneity in the applied bias magnetic field B_0 results in a residual gradient of less than 1.4 μT (40 kHz after accounting for the doubled gyromagnetic ratio in the DQ sensing basis). **(e)** Image of the SQ Ramsey fringe amplitude $A_0\{\mathrm{SQ}\}$ corresponding to the spin transition associated with the $m_I = 0$ nuclear spin state, in digital units (D.U.) as reported by the heliCam. **(f)** Image of the DQ Ramsey fringe amplitude $A_0\{\mathrm{DQ}\}$ corresponding to the spin transition associated with the $m_I = 0$ nuclear spin state, in digital units (D.U.) as reported by the heliCam.

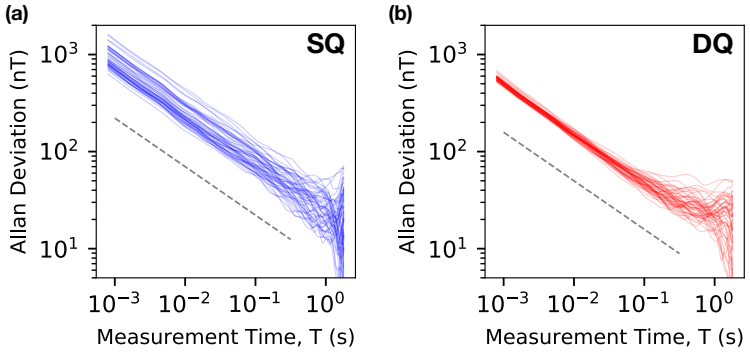
power law scaling proportional to $T^{-1/2}$, where T is the measurement time. The greater inhomogeneity in SQ magnetic sensitivities is apparent from the larger spread in SQ measurements compared to DQ measurements.

S8. AVERAGED MAGNETIC IMAGES

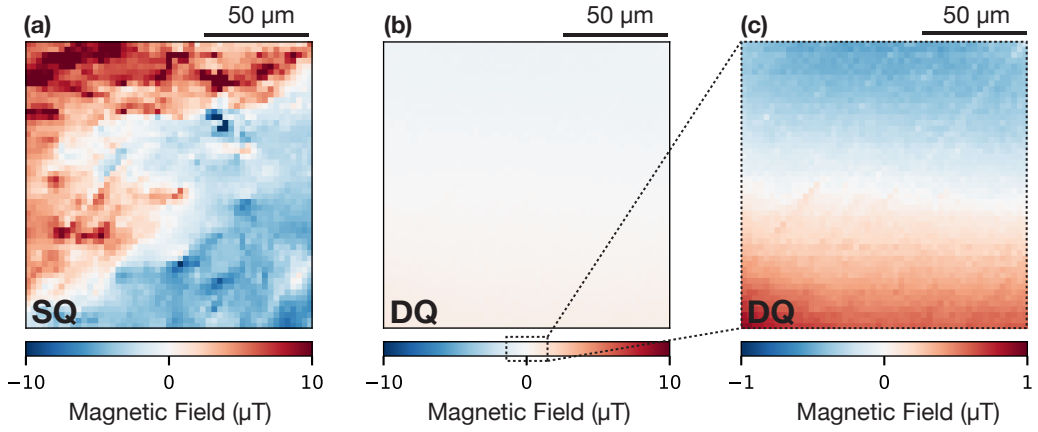
Figure S5 compares the magnetic field images produced after acquiring 1 second of data (each) using the SQ 2-Ramsey protocol and DQ 4-Ramsey protocols. No additional magnetic sources are applied beyond the 5 mT bias magnetic field. However, the SQ image in Fig. S5(a) exhibits large non-magnetic spatial variations on the

order of 10 µT due to axial-stress inhomogeneity. The inability of SQ measurements to distinguish axial crystal stress from magnetic fields complicates the analysis of such images and necessitates large measurement dynamic range (at the cost of magnetic sensitivity). In contrast, the pixels in the DQ image [Fig. S5(b)] respond only to magnetic-sources (to leading order), such that the resulting DQ image exhibits an order of magnitude reduced variation [as highlighted by the reduced color-scale in Fig. S5(c)].

The residual variation in the DQ magnetic image [Fig. S5(c)] is predominantly correlated with inhomogeneity in the bias magnetic field, which can be further engineered to reduce residual magnetic gradients. However, subtle scratch-like features on the sub-100 nT scale are also visible, stretching diagonally across the field of view. These features are attributed to damage on the surface of the diamond substrate before growth of the nitrogen-doped layer. Similar features can be identified in the extracted Ramsey fringe amplitudes in Figs. S3(c) and S3(d) for the SQ and, to a lesser extent, DQ sensing bases. The persistence of these features in both bases is informative and suggests that transverse-stress gradients, which are not suppressed by either sensing basis, may contribute to the residual variation of the averaged DQ image shown in Figs. S5(b) and S5(c) (see Supplemental Sec. 1).



Supplemental Figure S4. Allan deviations for magnetic field measurements as a function of measurement time. (a) Measurements using a SQ 2-Ramsey sensing protocol for 50 randomly selected pixels across the same field of view as used for measurements shown in Fig. 4 of the main text. (b) Measurements using the DQ 4-Ramsey sensing protocol for the same 50 pixels as depicted in (a). The free precession interval and detuning are optimized for each sensing basis to minimize the median per-pixel magnetic sensitivity. Dashed grey lines depict a power law scaling proportional to $T^{-1/2}$ as a guide to the eye.



Supplemental Figure S5. Averaged SQ 2-Ramsey and DQ 4-Ramsey images when operating at optimal sensing conditions across the same field of view as shown in Fig. S3 and S4. (a) SQ image exhibiting 10 μT-scale spatial variations due to stress-induced NV^- resonance shifts. (b) DQ image with reduced spatial variations due to insensitivity to non-magnetic sources. (c) Same data as (b) but with a 10× reduced magnetic field scale to highlight residual spatial variation predominantly correlated with the bias magnetic field, which is aligned along one NV^- axis at an angle of 54.7° relative to the normal to the image plane.

[S1] M. S. J. Barson, P. Peddibhotla, P. Ovartchaiyapong, K. Ganesan, R. L. Taylor, M. Gebert, Z. Mielens, B. Koslowski, D. A. Simpson, L. P. McGuinness, J. McCallum, S. Prawer, S. Onoda, T. Ohshima, A. C. Bleszynski Jayich, F. Jelezko, N. B. Manson, and M. W. Doherty, Nanomechanical sensing using spins in diamond, Nano Letters **17**, 1496 (2017).

[S2] P. Udvarhelyi, V. O. Shkolnikov, A. Gali, G. Burkard, and A. Pályi, Spin-strain interaction in nitrogen-vacancy centers in diamond, Phys. Rev. B **98**, 075201 (2018).

[S3] A. Barfuss, M. Kasperczyk, J. Kölbl, and P. Maletinsky, Spin-stress and spin-strain coupling in diamond-based hybrid spin oscillator systems, Phys. Rev. B **99**, 174102 (2019).

[S4] D. R. Glenn, R. R. Fu, P. Kehayias, D. Le Sage, E. A. Lima, B. P. Weiss, and R. L. Walsworth, Micrometer-scale magnetic imaging of geological samples using a quantum diamond microscope, Geochemistry, Geophysics, Geosystems **18**, 3254 (2017).

[S5] P. Kehayias, M. J. Turner, R. Trubko, J. M. Schloss, C. A. Hart, M. Wesson, D. R. Glenn, and R. L. Walsworth, Imaging crystal stress in diamond using ensembles of nitrogen-vacancy centers, Phys. Rev. B **100**, 174103 (2019).

[S6] N. Bar-Gill, L. M. Pham, A. Jarmola, D. Budker, and R. L. Walsworth, Solid-state electronic spin coherence time approaching one second., Nature communications **4**, 1743 (2013).

[S7] E. Bauch, C. A. Hart, J. M. Schloss, M. J. Turner, J. F. Barry, P. Kehayias, S. Singh, and R. L. Walsworth, Ultralong dephasing times in solid-state spin ensembles via quantum control, Phys. Rev. X **8**, 031025 (2018).